Predictive analytical modelling and experimental validation of processing maps in additive manufacturing of nitinol alloys

Zhu, Jia Ning; Borisov, Evgenii; Liang, Xiaohui; Farber, Eduard; Hermans, M. J.M.; Popovich, V. A.

DOI
10.1016/j.addma.2020.101802

Publication date
2021

Document Version
Final published version

Published in
Additive Manufacturing

Citation (APA)
Zhu, J. N., Borisov, E., Liang, X., Farber, E., Hermans, M. J. M., & Popovich, V. A. (2021). Predictive analytical modelling and experimental validation of processing maps in additive manufacturing of nitinol alloys. *Additive Manufacturing* , *38*, Article 101802. https://doi.org/10.1016/j.addma.2020.101802

Additive Manufacturing 38 (2021) 101802

Contents lists available at ScienceDirect

Additive Manufacturing

journal homepage: www.elsevier.com/locate/addma

Research Paper

Predictive analytical modelling and experimental validation of processing maps in additive manufacturing of nitinol alloys

Jia-Ning Zhu [a,*], Evgenii Borisov [b], Xiaohui Liang [a], Eduard Farber [b], M.J.M. Hermans [a], V. A. Popovich [a,b,**]

[a] Faculty of Mechanical, Maritime, and Materials Engineering, Delft University of Technology, The Netherlands
[b] Peter the Great Saint-Petersburg Polytechnic University, Saint Petersburg, Russia

ARTICLE INFO

Keywords:
Laser powder bed fusion
Nitinol alloys
Analytical model
Defect formation
Process optimization

ABSTRACT

Nitinol (NiTi) shape memory alloys fabricated by Laser Powder Bed Fusion (L-PBF) Additive Manufacturing (AM) have attracted much attention in recent years, as compared with conventional manufacturing processes it allows to produce Nitinol parts with high design complexity. Avoidance of defects during L-PBF is crucial for the production of high quality Nitinol parts. In this study, analytical models predicting melt pool dimensions and defect formation criteria were synergistically used to develop processing maps demonstrating boundary conditions for the formation of such defects, as balling, keyhole-induced pores, and lack of fusion. Experimental validation has demonstrated that this method can provide an accurate estimation and guide manufacturability of defect-free Nitinol alloys. Moreover, the crack formation phenomena were experimentally analysed, which showed that a low linear energy density (E_l) should be chosen to avoid cracks in the optimized process windows. Based on model predictions and experimental calibrations, Nitinol samples with a relative density of more than 99% were successfully fabricated.

1. Introduction

NiTi (i.e., Nitinol) shape memory alloys (SMAs) have a unique combination of shape memory capability, superelasticity (SE) and excellent bio-compatibility, making it an attractive material for various engineering and biomedical applications. NiTi-based SMAs display the largest deformation recovery of up to 8% are thus more utilized in most engineering applications [1,2]. However, it is well known that the fabrication of Nitinol components using conventional production methods is a challenge because of its high ductility, work hardening and reactivity [3,4]. Therefore, applications of Nitinol alloys are mainly limited to simple geometries including sheets, rods, wires and tubes [2].

Recently, the additive manufacturing (AM) technique, known as laser powder bed fusion (L-PBF), that employs CAD data to selectively melt the metal powder layer-by-layer by means of a laser beam, introduced more possibilities to fabricate a wide variety of complex and functional Nitinol parts [5–7]. This AM method allows to overcome conventional Nitinol fabrication problems and produce fully dense as well as porous or complex shaped internal and external structures. However, some defects such as balling, keyhole-induced pores, lack of fusion, and cracks may be introduced, due to not optimized processing parameters. Therefore, in order to take full advantage of L-PBF processing of high-quality parts, it is crucial to avoid defect formation. With the aim of a clear impression about different defects, the representative morphologies of these defects are shown in Fig. 1.

Above mentioned defects are tightly related to L-PBF processing parameters. Balling (Fig. 1(a)) mainly originates from the low laser energy input, which results in insufficient liquid and high surface tension within each laser bead. In this case, balling is introduced by increasing surface tension [8]. The lack of fusion (Fig. 1(b)) is either caused by the metallic powders that are not fully melted in the previous deposit layer (due to the lack of energy input) or too large hatch distance and/or layer thickness, which results in an insufficient overlap among the laser tracks [9]. In contrast, keyhole-induced pores (Fig. 1(c)) occurs in the high laser energy processing regime, when an unstable keyhole-shaped melt pool collapses on itself, trapping gas bubbles from the vapor depression [10]. Due to rapid melting and rapid solidification under a high local laser energy input, a great temperature gradient and as a result a large residual thermal stress can be created in the fabricated

* Corresponding author.
** Corresponding author at: Faculty of Mechanical, Maritime, and Materials Engineering, Delft University of Technology, The Netherlands.
E-mail addresses: J.Zhu-2@tudelft.nl (J.-N. Zhu), v.popovich@tudelft.nl (V.A. Popovich).

https://doi.org/10.1016/j.addma.2020.101802
Received 23 September 2020; Received in revised form 4 December 2020; Accepted 18 December 2020
Available online 29 December 2020

Nomenclature

L-PBF	Laser powder bed fusion	ρ	The density of material, kg/m^3
AM	Additive manufacturing	C_P	Heat capacity of material, J/(kg·K)
SMA	Shape memory alloy	T_m	The melting temperature, K
E_l	Linear energy density, J/mm	T_b	The boiling temperature, K
E_v	Volumetric energy density, J/mm^3	a	The radius of laser beam, μm
P	Laser power, W	σ	The Gaussian laser beam distribution parameter, μm
v	Scanning velocity, mm/s	k	The thermal conductivity of material, W/(m·K)
h	Hatch distance, mm	α	The thermal diffusivity, m^2/s
t	Layer thickness, μm	s	Time, s
D	Melt pool depth, μm	ρ_0	The electrical resistivity of the irradiated material, Ω/m
W	Melt pool width, μm	λ	The laser wavelength, nm
L	Melt pool length, μm	EDS	Energy-dispersive X-ray spectroscopy
ΔH	The specific enthalpy for evaluating keyhole formation, J/m^3	M_s	Martensite starting temperature, °C
		BR	Building rate of laser powder bed fusion, mm^3/s
h_s	The enthalpy at melting, J/m^3	f_w	The overlapping ratio of width between adjacent laser tracks
A	Laser absorptivity	f_D	The overlapping ratio of height between adjacent laser tracks

parts. Hence, the high temperature gradient combined with the high residual stress often causes cracking in a fabricated part (Fig. 1(d)) [9]. In addition, elemental segregation towards the grain boundaries may result in weak/brittle phases, thereby increasing the chance of micro-cracking [11].

In order to fabricate defects-free Nitinol samples, L-PBF process windows need to be established, which is typically achieved by a time and energy consuming trial and error approach [5,16,17]. For convenience, researchers have often introduced the energy density, which combines several main processing parameters, to evaluate the final part quality and have found that defects can indeed be minimized by adjusting the energy density range [18]. As reported by Oliveira et al.

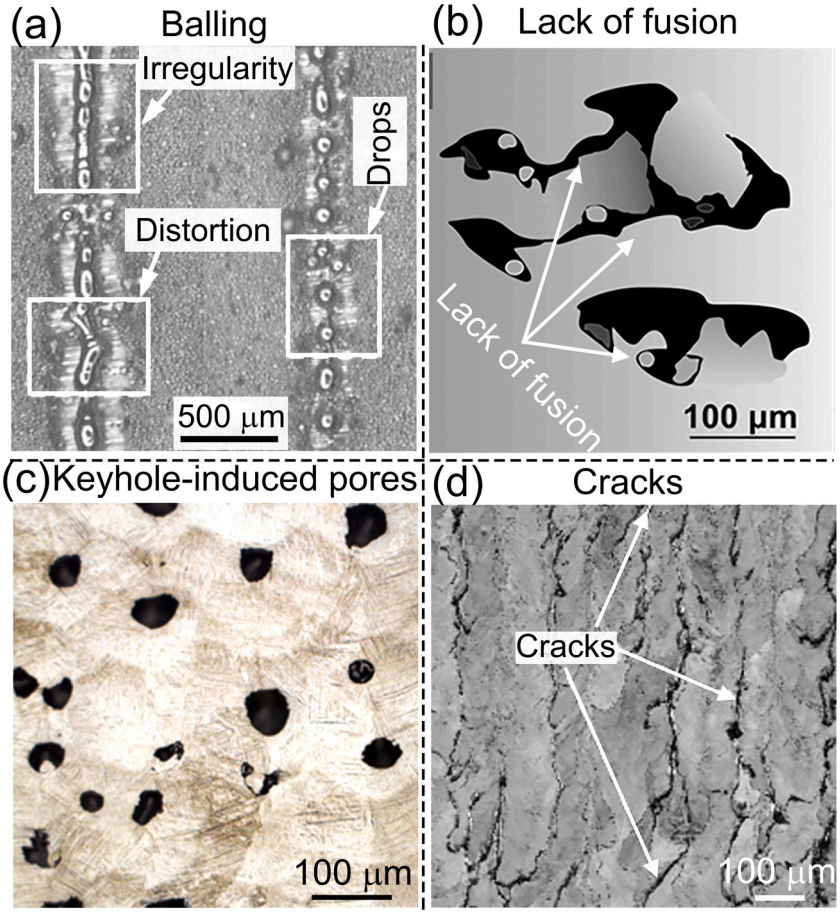

Fig. 1. Different defects in L-PBF parts: a. balling effect b. Lack of fusion c. Keyhole-induced pores d. cracks.
a. Reproduced with permission from [12] ©2010 Elsevier, The Netherlands. b. Reproduced with permission from [13] ©2019 John Wiley and Sons c. Reproduced with permission from [14] ©2016 Elsevier) d. Reproduced with permission from [15] ©2019 Elsevier.

[19], such two key process parameters as laser power and scanning velocity will affect maximum temperature of melt pools, which dictates the elemental evaporation, the amount of molten powders and the melt pool mode (conduction or keyhole mode). In order to control elemental evaporation and eliminate lack of fusion, an appropriate linear energy density (laser power to scanning velocity ratio) should be selected first and then layer thickness/hatch distance should be adjusted accordingly [19]. The linear energy density (E_l) can be represented by the ratio of laser power (P) and scanning velocity (v) and can be expressed as Eq. (1):

$$E_l = \frac{P}{v} \tag{1}$$

E_l is optimized to obtain desirable laser track shape, without the presence of balling and keyhole-induced pores [12,20–23].

For L-PBF process, the volume energy density (E_v) (the second type) is commonly used to describe the combined effect of main processing parameters including laser power (P, W), scanning velocity (v, mm/s), hatch distance (h, mm), and layer thickness (t, mm). This energy density quantifies the magnitude of energy input directed to the powder bed, and can be calculated using Eq. (2) [7,9]:

$$E_v = \frac{P}{v \cdot h \cdot t} \tag{2}$$

It has been shown that high quality Nitinol parts with a low defect density can be produced by L-PBF [24,25]. Optimization of L-PBF process parameters for fabrication of Nitinol parts has mainly been focused on determining the ideal volumetric energy density. As reported by Haberland et al. [26] and Meier et al. [27], the volumetric energy density of 85 J/mm^3 is the most optimal. However, Walker et al. [16] and Saedi et al. [28] argued that the volume energy density of approximately 55.5 J/mm^3 should be rather used to obtain fully dense L-PBF Nitinol alloys. In contrast, Dadbakhsh reported that high quality L-PBF Nitinol alloys can be fabricated with a high volumetric energy density of 111–126 J/mm^3 [29]. In the above mentioned energy densities, laser beam diameter and powder size were not considered. In order to develop a more generic definition of energy input during additive manufacturing, Oliveira et al. [30] proposed the Eq. (3) including all main process parameters:

$$ED = \beta \cdot \frac{P}{v \cdot h \cdot t}, \tag{3}$$

where β is the dimensionless parameter defined as the ratio of powder grain size (g_s) and the diameter of the laser beam ($d_{\text{Laser beam}}$). Since the same batch of NiTi powder and constant laser beam size were used in our work, the Eq. (2) was rather used to calculate the volumetric energy density.

Prashanth et al. pointed out that the energy density gives only an approximate estimation [31]. Bertoli et al. also argued the limitation of volume energy density for selecting L-PBF processing parameters, due to inability of the energy density approach to capture melt pool physics [18]. In fact, the quality of L-PBF samples depends on the quality of the individual laser track and the overlap between the adjacent laser tracks (melt pool depth-to-layer thickness (D/t) and melt pool width-to-hatch distance (W/h)) [31–33]. Therefore, it is not surprising that consensus is not reached regarding an optimal linear or volumetric energy density as criterion for estimating defect free L-PBF parts. In order to fabricate defect-free L-PBF Nitinol samples, melt pool dimensions and their tracks overlapping characteristics should be simultaneously considered.

Determination of processing conditions to achieve defect free components, including the effects of L-PBF processing parameters on the microstructural evolution and functional properties of L-PBF Nitinol alloys was previously addressed [6,24,28,34]. However, there is still no systemic investigation on the formation of defects induced by L-PBF processing of Nitinol parts. The presence of defects in L-PBF parts is a well-known drawback and a critical issue, which can deteriorate mechanical and functional properties of Nitinol alloys [5]. Therefore, it is essential to develop processing maps for L-PBF fabrication of high quality Nitinol parts and to investigate the effect of processing parameters on defect formation.

With the purpose of reducing laborious experimentation and achieving fast estimates of defects formation, the combination of melt pool dimensions based on analytical models and defect formation criteria has been proposed [33,35–37]. Seede et al. has proven the feasibility of combining the melt pool geometry and geometric criteria for avoiding defects formation (balling, keyhole-induced pores, and lack of fusion) and they have successfully fabricated an ultra-high strength martensitic steel using this method [27]. However, the approach relating melt pool dimensions and defects formation has not yet been applied to Nitinol alloys.

In this work, the analytic models are utilized to predict melt pool dimensions and L-PBF processing maps are further designed based on the relationship between melt pool dimensions and defect formation criteria. Finally, process parameters for Nitinol alloys are optimized and validated by fabrication of defect-free samples. Formation mechanisms of such defects as balling, keyhole-induced pores, lack of fusion and cracks are discussed in relation to L-PBF process parameters. Furthermore, micro-hardness and functional shape memory transformation properties of Nitinol alloys fabricated with various L-PBF processing parameters are investigated. Hence, the final aim of this work is to systematically understand the defect formation mechanisms and develop processing maps allowing to guide defect-free processability in L-PBF Nitinol parts.

2. Methodology

2.1. Defects formation and criteria

Balling effect, keyhole-induced pores and lack of fusion are three common types of defects in L-PBF components [38]. Defect formation criteria are mainly based on geometrical considerations and empirically determined values taken from the literature [12,18,33,37,39]. Apart from these common defects, crack formation may take place when stresses induced by the heat introduced by laser processing exceed the strength of the material.

Balling is caused by laser energy induced non-stable melt pools [40]. Generally, there are two kinds of balling phenomena during L-PBF. Low laser energy results in insufficient liquid and poor wetting, which contributes to the formation of discontinuous scan lines with coarsened ball formation (referred to the first kind of balling phenomenon). High laser scanning speed can cause liquid splashes (micrometer-scaled) onto cohesive powder particles, which is considered as the second kind of balling phenomenon [22]. Due to large irregularities, distortion, and drops in the first kind of balling phenomenon, mechanical properties and the melt pool overlapping can be significantly affected [38]. Therefore, in particular the first kind of balling should be avoided during L-PBF and will be the main defect considered in our work.

For the formation of first kind of balling formation, Yadroitsev et al. have proven that melt pool stability can be evaluated by the ratio of melt pool width (W) to its length (L) [12]. The necessary condition for the melt pool stability is:

$$\frac{\pi W}{L} > \sqrt{\frac{2}{3}} \tag{4}$$

When excess energy is introduced by the laser, melt pools are formed in the keyhole mode [41]. Keyhole-induced pores can be caused by the entrainment of shielding gas, collapse of unstable keyholes, or premature solidification of the top surface [42,43]. These pores cause stress concentration and have a negative effect on mechanical properties [44,45]. Formation of keyhole-induced pores is a complex multi-physics process and a numerical framework based on the commercial software FLUENT has been proposed by We et al. [46], which successfully

interprets the dynamic process of keyhole-induced pore formation and provides a solution to decrease porosity. King et al. have demonstrated that the depth of the melt pool has a linear relationship with the normalized enthalpy, and the keyhole-induced pore formation can be estimated by a criterion given in Eq. (5) [18]:

$$\frac{\Delta H}{h_s} = \frac{AP}{\pi h_s \sqrt{\alpha v a^3}} > \frac{\pi T_b}{T_m} \tag{5}$$

where $\frac{\Delta H}{h_s}$ is the normalized enthalpy, ΔH (J/m^3) is the specific enthalpy, $h_s = \rho C_p T_m$ (J/m^3, ρ is the density and C_p is the heat capacity (J/(kg·K))) is the enthalpy at melting, A is laser absorptivity, α is the thermal diffusivity (m^2/s), v is scanning velocity (mm/s), T_m melting temperature (K), and T_b is boiling temperature (K). In order to evaluate keyhole-induced pore formation during L-PBF, the 1/e radius (the resulting laser beam radius at which energy density is minimized to 1/e at the center of the laser beam) of the laser beam is treated as the laser spot size ($a = \sqrt{2}\sigma$, with σ the Gaussian laser beam distribution parameter) [41].

Lack of fusion is a planar defect which occurs when insufficient heat is available to create an appropriate bonding between the newly deposited bead and the prior layers. When laser power, spot size and scanning speed (i.e. linear energy density) are selected, this type of defect results from inappropriate combination of hatch distance (h), layer thickness (t), melt pool width (W) and depth (D). The hatch distance h is defined as the distance between the centre lines of adjacent tracks (indicated in Fig. 2(b)).

In order to avoid lack of fusion, a maximum hatch distance should be adjusted to ensure the good joining between the adjacent tracks [30]. The criteria for the maximum hatch distance have been proposed from geometric, energetic and thermal aspects [30]. In this work geometric criterion was used for its simplistic calculations, allowing to build relationships between process parameters and melt pool dimensions.

As proposed by Seede et al. [33], lack of fusion may occur for melt pools featuring parabola-shaped cross-sections, when h exceeds the maximum hatch distance h_{max},. The h_{max} can be calculated based on Eq. (6):

$$h_{\max} = W\sqrt{1 - \frac{t}{(t+D)}}. \tag{6}$$

Therefore, the criterion for lack of fusion can be described by the Eq. (7), which is derived from Eq. (6):

$$\left(\frac{h}{W}\right)^2 + \frac{t}{(t+D)} \geq 1. \tag{7}$$

2.2. Melt pool dimension calculations

As stated above, it is necessary to obtain melt pool dimensions for the evaluation of defects formation. Compared with finite-element model (FEM), analytical solutions are considered as simple and computationally inexpensive methods for predicting melt pool dimensions [33,37,47]. Eagar-Tsai (E-T) model has been proven to be an effective analytical model, which can provide a reasonable accurate estimation of the melt pool width and length [33,35,36,48]. In the Eagar-Tsai model [49], a Gaussian distributed heat source is assumed, allowing to solve the differential equation analytically to obtain the temperature distribution and hence to achieve the melt pool profile. Based on the Eagar-Tsai model, the analytical form is re-derived as Eq. (8):

$$T = \frac{AP}{\pi k}\sqrt{\frac{\alpha}{\pi}}\int_0^{\infty} \frac{\exp\left[-\frac{z^2}{4\alpha s} - \frac{y^2+(x-vs)^2}{(4\alpha s + a_1^2)}\right]}{(4\alpha s + a_1^2)\sqrt{s}} ds \tag{8}$$

where k is the thermal conductivity (W/(m·K)),$\alpha$is the thermal diffusivity (m^2/s), s is the time (s), $a_1$is the radius of beam size ($a_1 = \sigma$,$\sigma$is the distribution parameter of the Gaussian distributed heat source). The scanning direction of the laser beam is along x and y in the transverse coordinate, and z is directed normal to the substrate surface.

For the convenience of the melt pool dimension calculations, the Eq. (8) can be put in dimensionless form by using the following dimensionless variables: $x_N = \frac{x}{a_1}; y_N = \frac{y}{a_1}; z_N = \frac{z}{\sqrt{\left(\frac{\alpha a_1}{v}\right)}}$ [36]. Furthermore, the parameter g, which is independent of laser and material parameters, is introduced to describe the effect of scanning speed (v) on the temperature distribution [48]. Therefore, dimensionless variables and temperature distribution are expressed as follows in Eqs. (9) and (10) [48]:

$$T = T_S g(x_N, y_N, z_N, v) \tag{9}$$

$$g\left(x_N, y_N, z_N, v\right) = \int_0^{\infty} \frac{\exp\left[-\frac{z_N^2}{4\tau} - \frac{y_N^2+(x_N-\tau)^2}{\left(\frac{\alpha\tau}{va_1}+1\right)}\right]}{\left(\frac{\alpha\tau}{va_1}+1\right)\sqrt{\tau}} d\tau \tag{10}$$

where, $T_S = \frac{AP}{\pi\rho C_p \sqrt{\alpha v {a_1}^3}}$is the surface temperature, while the melt pool contour is determined from the condition that T equals the melting point of the material. $T = T_m$ (T_m is the melting point of material) and $\tau = \frac{s}{\left(\frac{a_1}{v}\right)}$is the dimensionless time. The readers were encouraged to refer to

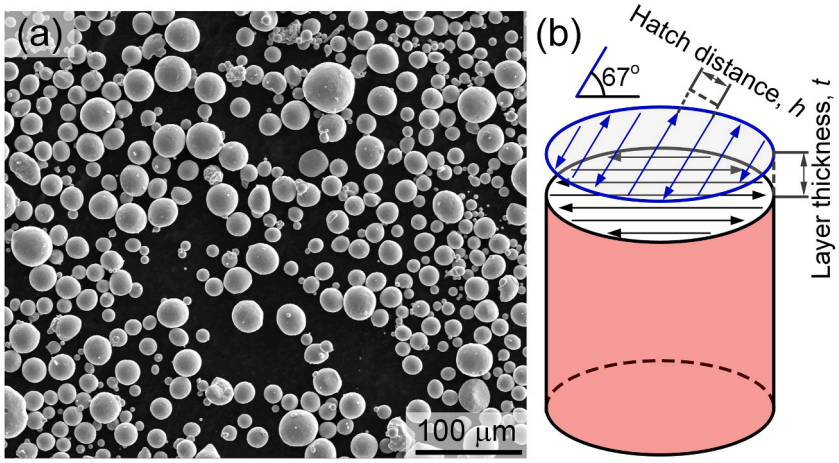

Fig. 2. (a) SEM of the commercial Nitinol powder and (b) the schematic of the applied L-PBF scanning strategy.

the original study for more details about the development of thermal analytical solution [48].

Due to the fact that the E-T model is designed to investigate heat conduction-mode laser melting [35], the depth of melt pool will be underestimated by the change of the melt pool shape from the conduction mode melting to the keyhole mode melting [50]. An alternative model proposed by Gladush and Smurov, i.e. the G-S model, [39] is a good candidate for predicting melt pool depth, since it was derived for investigating keyhole welding, which is consistent with the purpose of this work. Melt pool depth (D) can be described as a function of laser power (P), scanning speed (v) and laser beam size (a_1) (as shown in Eq. (11)):

$$D = \frac{AP}{2\pi k T_b} \ln\left(\frac{a_1 + \alpha/v}{a_1}\right) \tag{11}$$

where A is laser absorptivity, k is the thermal conductivity (W/(m·K)), T_b is the boiling temperature (K), and α is the thermal diffusivity (m^2/s).

2.3. Model parameters

Due to the preheating from neighboring laser tracks during L-PBF, the temperature and phase dependence of physical parameters should be considered. As reported by Ma et al. [6], the temperature of neighboring tracks can reach near the melting point during fabrication of Nitinol parts. Therefore, temperature dependent properties at 1500 K (near the melting point), such as density and thermal diffusivity, were used in our work. Due to the lack of the experimental density data for Nitinol, the density as a function of temperature is calculated by using Thermo-Calc software (Version 2020a) based on TCHEA2 (High Entropy Alloys version 2.1) database. Considering the fact that the crystal structure of the Nitinol alloy is austenitic at high temperature [51], the heat capacity of austenitic Nitinol is used in our work.

According to Drude's theory [32], the laser absorptivity A used in L-PBF can be estimated by using empirical Eq. (12) [32]:

$$A = 0.365\sqrt{\left(\frac{\rho_0}{\lambda}\right)} \tag{12}$$

where ρ_0 (Ω/m) is the electrical resistivity of the irradiated material and λ (nm) is the laser wavelength. Based on Eq. (12), the laser absorptivity of Nitinol is 0.32, which is similar with that of Ti ($A_{Ti} = 0.36$) [52] and Ni-based alloys ($A_{Inconel\ 718} = 0.38$) [53]. Nitinol properties and laser-related parameters are listed in Table 1.

2.4. L-PBF fabrication

The Nitinol samples were fabricated via L-PBF process by an Aconity3D Midi (Aconity3D GmbH, Germany) machine equipped with a laser source featuring a maximum power of 1000 W and a beam with a Gaussian distribution. Gas atomized Nitinol powder (TLS Technik GmbH, Bitterfeld, Germany) with ~50.0 at% content of Ni and spherical particles with D-values of 23 μm (D_{10}), 40 μm (D_{50}), 67 μm (D_{90}) was used in this study (Fig. 2(a)). Chemical composition of Nitinol powder was measured by a combination of Energy-dispersive X-ray spectroscopy (EDS), Inductively Coupled Plasma Optical Emission Spectroscopy (ICP-OES) and LECO combustion analysis and was confirmed to be Ni50.0 (at %)–Ti with negligible impurity content (C, N, and O).

Table 1
Nitinol thermal physical properties and laser related parameters used in the analytical solution at 1500 K.

Density (kg/m^3), ρ	6100
Heat capacity (J/(kg·K)), C_p	510 (austenite)[54]
Thermal conductivity (W/(m·K)), k	4.4[55]
Thermal diffusivity (m^2/s), α	8e-6[56]
Electrical resistivity (Ω/m), ρ_0	8.2e-8 (austenite)[57]
Melting temperature (K), T_m	1583
Boiling temperature (K), T_b	3033[58]
Laser beam radius (μm), a_1	40
Laser wavelength (nm), λ	1070
Absorptivity, A	0.32

As shown in Fig. 2(b), a bidirectional scanning strategy was conducted in each layer and a 67° scanning rotation between the adjacent layers was applied. When altering the scanning direction from layer to layer by 67°, it results in an increase of intertwined grain boundaries and thus inhibits the initiation and propagation of cracks [15]. L-PBF cylindrical samples (diameter of 6 mm and height of 20 mm) were fabricated on a Nitinol base plate in Argon protection atmosphere. The volume energy density (E_v) was defined by Eq. (2). In this work, the constant laser power of 250 W and laser beam size of 80 μm (diameter) were used, while the hatch distance, layer thickness and scan velocity were varied, as shown in test groups A1–A9 in Table 2.

Process parameters were selected to investigate effects of linear and volumetric energy density, hatch and layer distances on defect formation.

2.5. Characterization

The relative density of the fabricated L-PBF samples was determined by the Archimedes method, using a theoretical maximum density of 6.45 kg/m^3. Samples for metallographic examination were ground, polished and etched in a reagent of HF (3.2 vol%) + HNO_3 (14.1 vol%) + H_2O (82.7 vol%) for ~ 50 − 70 s [28]. The etched microstructure was examined using an optical microscope (OM, Keyence VHX-5000) and a scanning electron microscope (SEM, JEOL JSM 6500 F) equipped with dispersive X-ray spectroscopy (EDS) analyser. Phase transformation behaviour was analysed by a differential scanning calorimetry (DSC, Perkin Elmer DSC 800) with a cooling and heating rate of 10 K/min over a temperature range of 213–473 K. A sample of approximately 100 mg was sliced from the middle of L-PBF-Nitinol samples for DSC analysis. Vickers hardness measurements were performed under the test force 0.3 kgf (further denoted as HV0.3) using an Automatic MicroHardness Tester (Buehler Vickers). In order to measure Ni content of bulk samples, at least 7 rectangular zones (180 × 250 μm^2, at 500× magnification) were measured by EDS (15 kV, beam current medium 13) on polished cross-sections and error bars were determined by calculating the standard deviation based on EDS results.

3. Results and discussion

3.1. Analytical prediction of the melt pool dimensions

By solving Eqs. (9) and (13), temperature contour can be plotted by using dimensionless (normalized) term g. An example of a temperature contour plot and the melt pool boundary (indicated by the black line) with the heat input resulting from 250 W laser power and 1250 mm/s scanning velocity is shown in Fig. 3(a). Based on the thermal results from the analytical solution of the E-T model, melt pool dimensions can be calculated. The melt pool width and length as functions of laser power (P) and scanning speed (v) are shown in Fig. 3(b) and (c), respectively. It can be seen that the melt pool width and length increase with increasing laser power or decreasing scanning speed (Fig. 3(b) and (c)), which means that both P and v are parameters significantly affecting the melt pool configuration and the thermal field within each laser track.

To verify the accuracy of the E-T model, experimental validations were carried out. Fig. 4(a) illustrates the applicability of E-T model for predicting melt pool widths, while Fig. 4(e)–(h) shows experimental results of the melt pool widths, which, as can be seen, match well with the values obtained from the analytical solutions. The minimum and maximum prediction error of melt pool width are ~3% and ~9%, respectively, which indicates reasonable accuracy of E-T model for

Table 2
L-PBF process parameters used for the fabrication of Nitinol samples.

	A1	A2	A3	A4	A5	A6	A7	A8	A9
Laser Power (W)	250	250	250	250	250	250	250	250	250
Scan velocity (mm/s)	1250	1250	1250	800	800	500	600	500	800
Hatch distance (μm)	100	120	140	120	140	140	140	120	187
Layer thickness (μm)	30	30	30	30	30	60	30	75	30
Laser beam diameter (μm)	80	80	80	80	80	80	80	80	80
Volumetric energy density (J/mm^3)	67	56	48	87	74	60	99	56	56

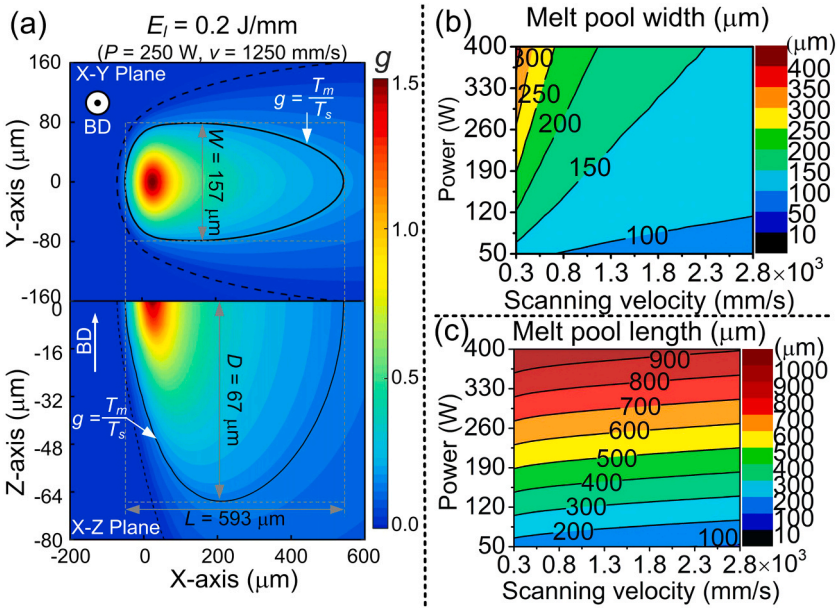

Fig. 3. (a) Cross-sectional views (X-Y and X-Z planes) of the temperature contour (plotted by g) and the melt pool boundary (indicated by the black solid line, where $g = \frac{T_m}{T_s}$) from the E-T model; (b) melt pool width and (c) length as the function of the laser power and scanning velocity.

predicting melt pool widths. Fig. 4(b) shows that the E-T model (a red dashed line with solid rod symbol) underestimates the melt pool depth, which is consistent with results reported in the literature [33,35,36]. Since The Eagar-Tsai model is designed to describe conduction-mode laser melting and assumes constant thermophysical properties (ρ,C_P and k), it hard to obtain accurate melt pool depth estimation if L-PBF change from heat conduction to keyhole-mode, characteristic to the high energy input condition. In order to achieve reasonably accurate estimations of the melt pool depth, Eq. (11) proposed by Gladush and Smurov (G-S model) for keyhole welding is used in our work. As shown in Fig. 4(b), the G-S model (a violet dashed line with open circles) has a better accuracy than the E-T model for predicting melt pool depths. The maximum deviation between the depth predicted by G-S model and experimentally measured depth is ~23%, which is substantially lower than ~50% deviation found for the E-T predicted depth. Therefore, the G-S model is further used for predicting melt pool depths. Melt pool depths predicted by the G-S model with various laser power and scanning velocity are shown in Fig. 4(c).

The criterion for keyhole-induced pore formation is determined by the normalized enthalpy $\frac{\Delta H}{h_s}$. The process map for keyhole-induced pore formation, based on Eq. (5) is presented in Fig. 4(d). As shown in Fig. 4 (d), Nitinol samples may exhibit keyhole-induced pore for scanning velocities up to 500 mm/s in a condition of constant laser power of 250 W, which is consistent with our experimental results (Fig. 4(h), keyhole-induced pores are marked by black dashed circles). It should be noted, that although keyhole-induced pore formation with its physical complexity is hard to be precisely described by the simple analytical equation (Eq. (5)), the approach by evaluating normalized enthalpy appears to be a simple and a rather good estimation.

Due to the difficulty of measuring the melt pool length and a lack of available data from the literature, it is hard to conduct a direct comparison between calculated and experimental results. As reported by Prompoppatum et al. [36], if only room temperature thermal properties are used in the E-T model and there is a positive correlation between temperature and thermal diffusivity, the melt pool length will be overestimated. They proposed a correction factor to compensate for the lack of temperature-dependent properties and thus the prediction accuracy of melt pool lengths was improved [36]. Following a similar strategy and considering the fact that powder surrounding a melt pool has the temperature close to the melting point [6], high temperature (1500 K near the melting point) thermal properties of Nitinol were used in the E-T model to improve the prediction accuracy. The validation of the melt pool length is discussed further in Section 3.3, in combination with the balling phenomena.

3.2. Processing maps and experimental validation

As stated above, the analytical approaches can provide a reasonably accurate estimation of the melt pool dimension and the occurrence of keyholing. Therefore, processing maps for the L-PBF of Nitinol alloys can be drawn by combining the defect formation criteria introduced in Section 2.1 and the melt pool dimensions predicted by the analytical approaches.

Processing maps with four linear energy density conditions are depicted in Fig. 5. The experimental results of Nitinol samples fabricated with various processing conditions, see Table 2, are indicated in the Fig. 5.

According to these processing windows (Fig. 5), the laser power

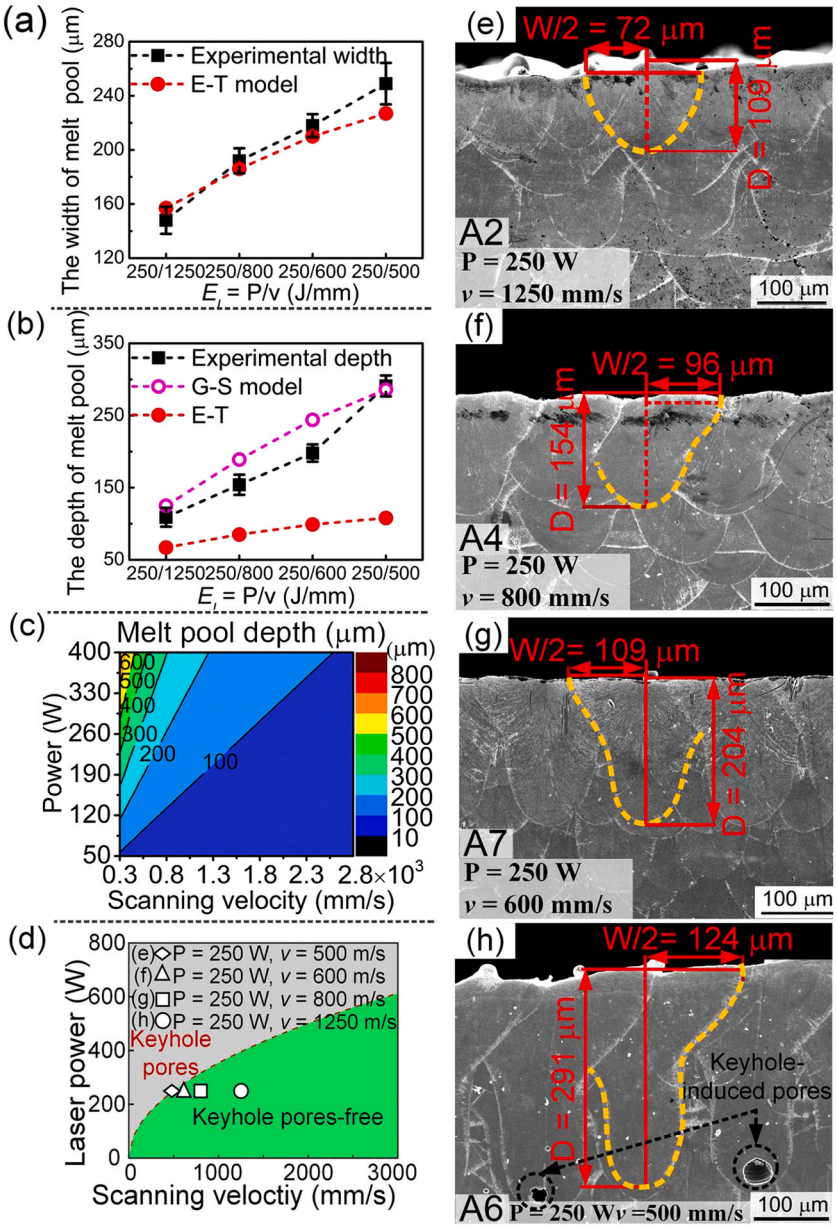

Fig. 4. Comparison of the experimentally measured melt pools (a) widths and (b) depths between the E-T model and the G-S model predictions; (c) melt pool depths as a function of the laser power and scanning velocities based on the G-S model; (d) the process map for keyhole-induced pore formation; (e)-(h) cross-sectional L-PBF Nitinol fabricated by the same laser power and different scanning velocities showing melt pool characteristics (For the interpretation of the color references featured in this figure legend, the reader is referred to the web version of this article).

should be in the range of 50–320 W to allow the fabrication of fully dense Nitinol parts. Apart from creating defect free parts, the build rate (BR) should also be considered. The build rate (BR) can be expressed as:

$$BR = v \cdot h \cdot t \tag{13}$$

Based on Eq. (2), i.e. the volumetric energy density (E_v), a higher BR can be achieved when using a higher laser power for the condition of a constant E_v. Therefore, with respect to the balance śof the high building rate and process reliability, a laser power of 250 W is chosen in our work.

Based on the defect criteria introduced in Section 2.1, both keyhole-induced pores and balling mainly depend on the heat-input related parameters (laser power, scanning velocity and laser beam size) and thermal physical properties. For Nitinol and constant laser beam diameter of 80 μm, regimes of keyhole-induced pores and balling can be determined by laser power and scanning velocity. Hence, there are fixed regimes for keyhole-induced pores (the upper-left corner) and balling (the upper-right corner), as shown in Fig. 5.

The lack of fusion is determined by melt pool dimensions (related to laser power and scanning velocity), hatch distance and layer thickness. Therefore, these parameters can be used to determine lack of fusion boundaries in the processing maps (as can be seen in Fig. 5).

Fig. 5(a) shows that the fully dense region has narrowed with increasing hatch distance (from 100 to 140 μm) while keeping a constant layer thickness of 30 μm. Samples A1, A2 and A3 share the same position in the processing map (Fig. 5(a)), since these were fabricated with the same laser power of 250 W and a scanning velocity of 1250 mm/s. Sample A3 (circled out in the solid green region, Fig. 5(a)) is near the boundaries of balling and lack of fusion.

Fig. 5(b) shows a processing map of samples A4, A5 and A9 with varying hatch distance from 120 to 187 μm and a lower scanning velocity of 800 mm/s (compare to 1250 mm/s in Fig. 5(a)). As can be seen, the fully dense area decreases with increasing hatch distance. The sample A9 falls into the lack of fusion regime (solid green region surrounded by the black dash line in Fig. 5(b)).

As shown in Fig. 5(c), boundaries for fully dense region can be determined (the solid green region) once hatch distance and layer thickness are selected. Positions of A3, A5 and A7 depend on the applied

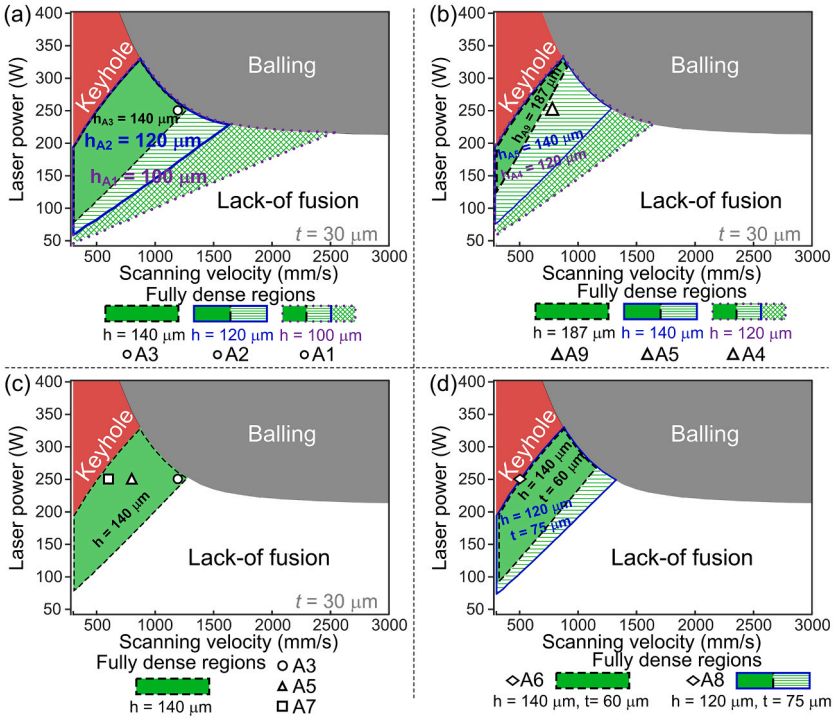

Fig. 5. Processing maps for L-PBF of Nitinol featuring locations of experimental data of samples fabricated with various processing parameters (For interpretation of the color references featured in this figure legend, the reader is referred to the web version of this article).

linear energy densities.

A processing map corresponding to simultaneous changes of hatch distance and layer thickness is shown in Fig. 5(d). The fully dense region of h = 120 and t = 75 μm is indicated by the blue line (Fig. 5(d)) and that of h = 140 and t = 60 μm is indicated by the black dash line (Fig. 5 (d)). Samples A6 and A8 (sharing the same position in the processing map and marked by a white diamond) are fabricated with a high linear energy density 250/500 (J/mm) and are both susceptible to keyhole-induced pore formation (Fig. 5(d)).

In order to quantitatively evaluate densification of L-PBF NiTi parts, the threshold of 99% relative density is defined as a good densification level [59]. As seen in Fig. 6, good densifications can be obtained in sample A2 and A8 with E_v of 56 J/mm^3 and A7 with E_v of 99 J/mm^3. These results demonstrate that the volumetric energy density can act as a rough guide in fabrication of dense Nitinol parts. However, the suitability of E_v as a design parameter to describe L-PBF is limited due to its low accuracy on estimating relative density of L-PBF parts.

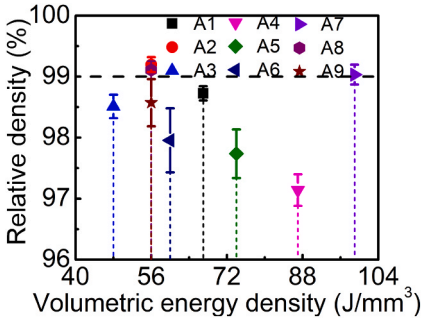

Fig. 6. Measured relative density of L-PBF Nitinol samples, fabricated with various processing parameters as a function of volume energy input (the threshold of 99% relative density is marked by the black dash line for defining a good densification level).

3.3. Characterization of balling phenomena

Balling is a typical L-PBF process defect [5,22]. Since L-PBF is carried out line-by-line and layer-by-layer. The balling may lead to discontinuities in the laser beads and may hinder the uniform deposition of subsequent powder layers [22]. Therefore, the factors affecting balling should be carefully considered for process optimization.

Fig. 7 shows the top surface of samples A1–A3 produced with the same linear energy density (250/1250 J/mm), but with various hatch distances. Laser tracks with small-sized balling and small gaps can be seen in A3 (with a hatch distance of 140 μm) (Fig. 7(c)), which means that the linear energy density of 250/1250 (J/mm) and hatch distance of 140 μm is near the boundary of balling initiation. The result is also consistent with our prediction (Fig. 5(a)). Thus, the feasibility of analytical melt pool dimension prediction on the estimation of balling effect is justified.

As shown in Fig. 7, balling effect can be well alleviated via narrowing the hatch distance. The balling effect in samples A3 can be attributed to the constant laser power (250 W) combined with a high scanning velocity (1250 mm/s, compared with other samples A4–A9), causing melt pool instabilities, where the melt tends to have a large surface energy. Hence, rough laser tracks consisting of a number of small-sized balls are formed. Due to increased overlapping ratios (Fig. 7(d)), induced by reducing hatch distance, energy input increases and re-melt of previous tracks is enhanced, which can decrease the viscosity of the melt (the overlapping ratio of width is defined as $f_w = \frac{W-h}{W}$ and the overlapping ratio of height is defined as $f_D = \frac{D-t}{D}$, where W is the width of melt pool, h is hatch distance, D is the height of melt pool and t is the layer thickness). Therefore, the balling tendency can be decreased with narrowing the hatch distance.

For a better understanding of balling phenomena in L-PBF Nitinol alloys, samples with various hatch distance (Fig. 5(b)) and linear energy density (Fig. 5(c)) were fabricated. As illustrated in the predicted process map (Fig. 5(b)), it is possible to avoid keyhole-induced pores and balling by using processing parameters with a laser power of 250 W and scanning velocity of 800 mm/s. As expected, with increasing the linear

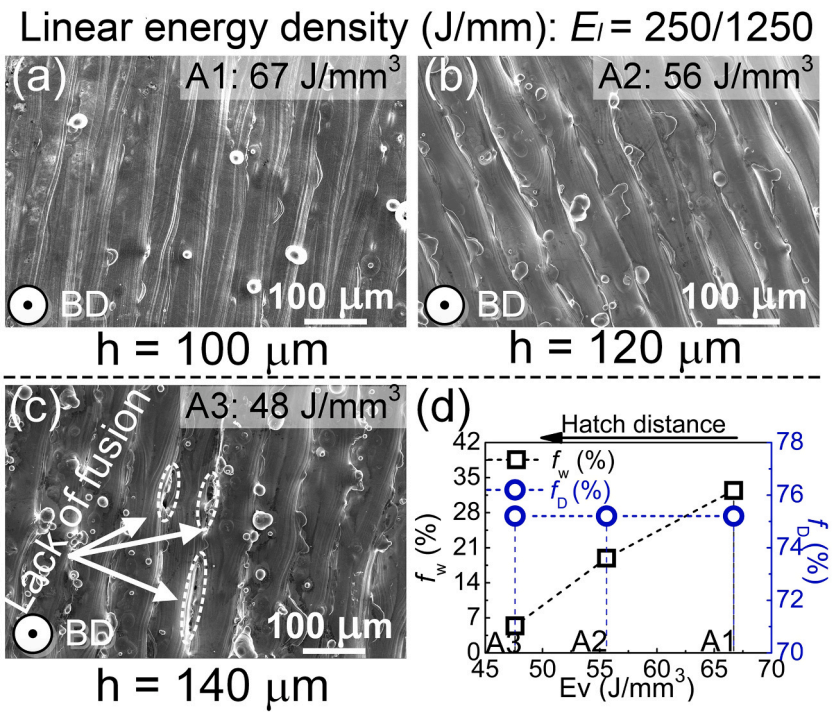

Fig. 7. SEM micrographs of the top surfaces of L-PBF Nitinol fabricated with the same linear energy of 250/1250 J/mm, but various hatch distances: (a) 100, (b) 120 and (c) 140 μm, (d) overlapping ratios of the melt pool width and height for samples A1–A3.

energy density, enabled by decreasing scanning velocity (Fig. 8(a)–(f)), continuous and balling-free laser tracks are produced, which is due to a sufficient liquid formation and a decrease of the melt viscosity [22]. It should however be noted that, although balling phenomena was eliminated, the cracks are introduced. Similar with the effect of hatch distance on balling phenomena of Nitinol samples fabricated by linear energy density of 250/1250 (J/mm), the balling effect is also alleviated with decreasing hatch distance in Nitinol samples fabricated by 250/800 (J/mm) (Fig. 9(a)–(f)). However, there are still cracks in the A4 sample (with narrowing hatch distance to 120 at E_l of 250/800 (J/mm), Fig. 9 (a) and (d)). Considering the serious negative effect of cracks in AM parts, especially with respect to limiting functional properties, fatigue life and fracture toughness, cracks should be always avoided [5,60]. Therefore, the linear energy density E_l of 250/1250 (J/mm) was optimized in the current work and balling were controlled by narrowing the hatch distance. Crack formation in L-PBF Nitinol parts will be discussed in Section 3.6.

3.4. Keyhole-induced pores

In Section 3.1, it has been demonstrated and validated that keyhole-induced pores form in the condition of high linear energy density (i.e. a high laser power and a low scanning velocity). In order to estimate the effect of hatch distance and layer thickness on keyhole-induced pores, cylindrical Nitinol samples were fabricated with various hatch distance and layer thickness, but a constant linear energy density of 250/500 J/

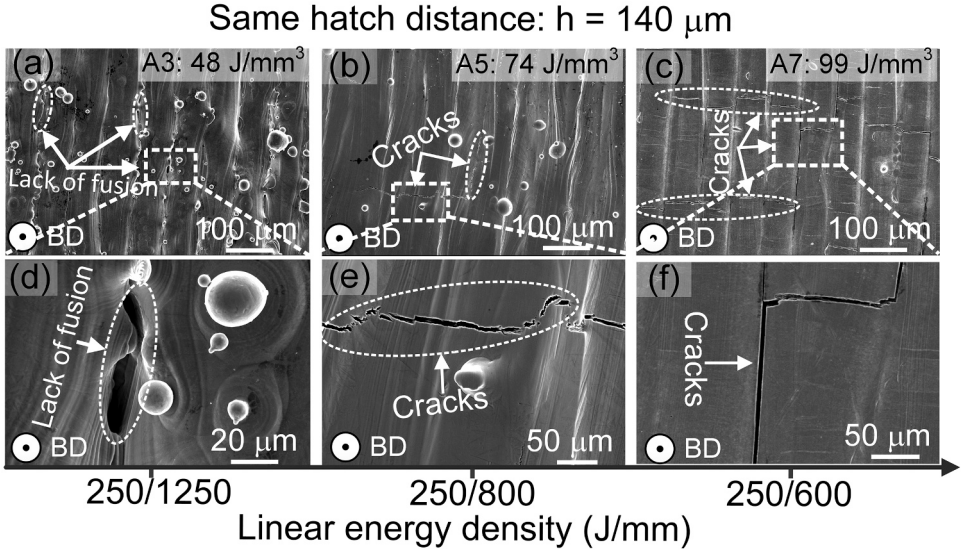

Fig. 8. SEM images of the top surfaces of L-PBF Nitinol alloys fabricated with various linear energy densities but a constant hatch distance 140 μm: (a) and (d) sample A3 with E_l = 250/1250 (J/mm); (b) and (e) sample A5 with E_l = 250/800 (J/mm); (c) and (f) sample A7 with E_l = 250/600 (J/mm).

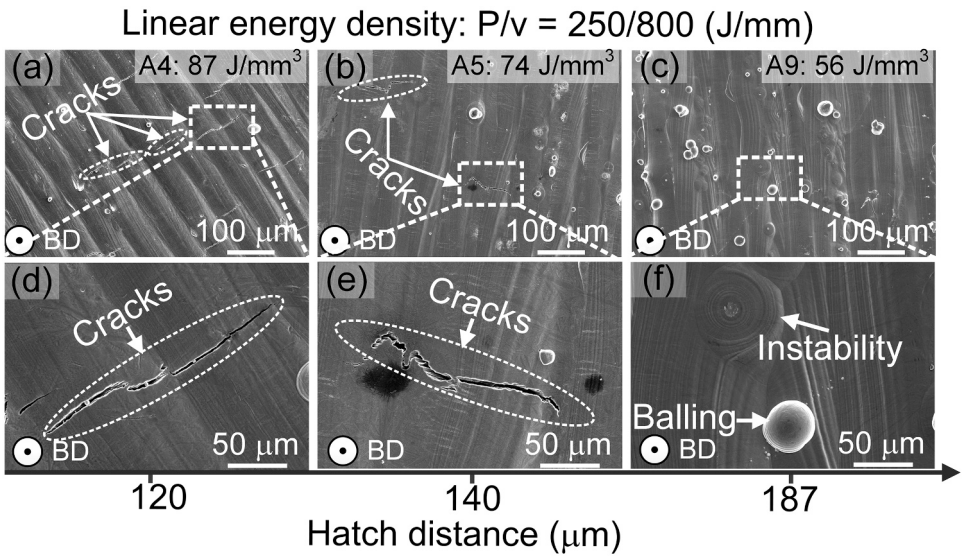

Fig. 9. SEM images of the top surfaces of L-PBF Nitinol alloys fabricated with various hatch distances but a constant linear energy density of 250/800 (J/mm): (a) and (d) sample A4 with h = 120 μm; (b) and (e) sample A5 with h = 140 μm; (c) and (f) sample A9 with h = 187 μm.

mm (in the keyhole-induced pores region, Fig. 5(d)). It can be seen that keyhole-induced pores and cracks are presented in sample A8 with hatch distance of 120 μm and layer thickness of 75 μm (Fig. 10 (a), (c) and (e)). With increasing hatch distance to 140 μm and decreasing layer thickness to 60 μm, keyhole-induced pores still can be observed in sample A6 (Fig. 10 (d) and (f)). Hence, it is demonstrated that heat input related

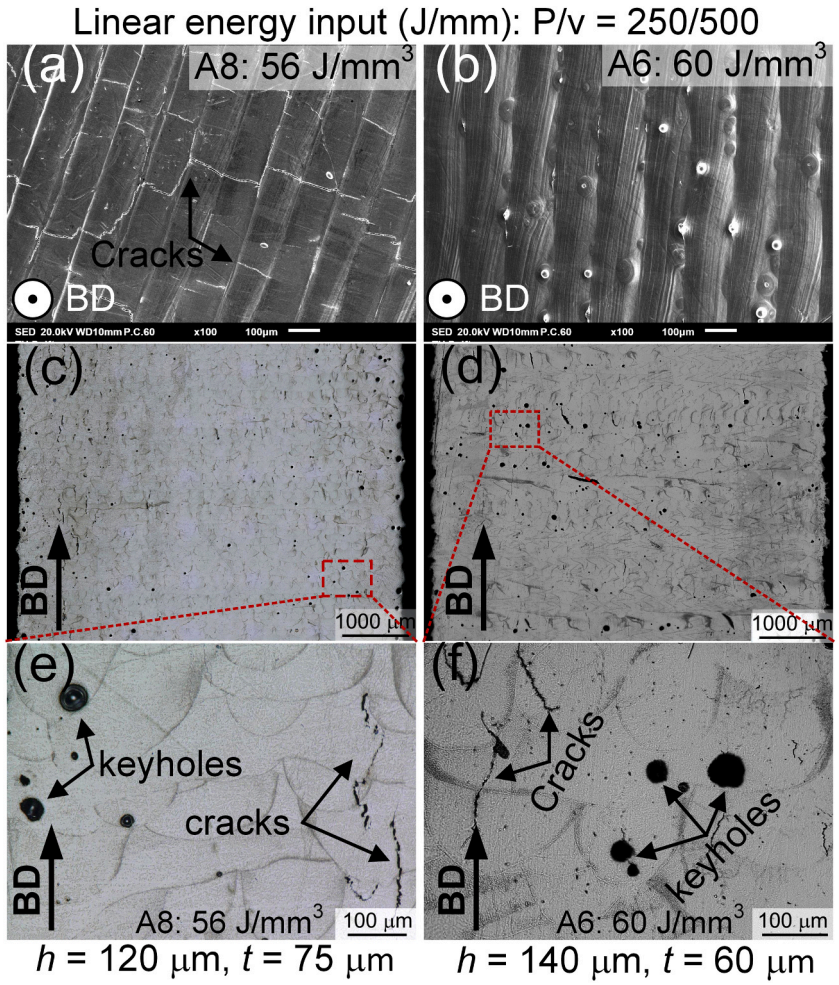

Fig. 10. SEM of L-PBF Nitinol alloys fabricated with the same linear energy level of 250/500 J/mm, but various hatch distance and layer thickness: (a), (c) and (e) h = 120 μm, t = 75 μm and (b), (d) and (f) h = 140 μm, t = 60 μm.

parameters (laser power and scanning velocity) are main factors affecting keyhole-induced pore formation and thus should be carefully chosen. Moreover, although the degree of cracking is reduced, the balling phenomenon is exacerbated in sample A6 (Fig. 10 (b)), which indicates the importance of hatch distance on cracks formation and balling effect. Based on characterization of samples A6 and A8, the reliability of processing map for predicting keyhole-induced pores is thus further confirmed (samples A6 and A8 in the keyhole-induced pore regime, Fig. 5(d)). Therefore, keyhole-induced pores are mainly dependent on heat input related parameters (laser power and scanning velocity), which should be chosen carefully to avoid introducing an excessive energy in melt pools.

3.5. Lack of fusion

As can be seen in Fig. 7(c) and Fig. 8(a) and (d), lack of fusion occurs in sample A3 fabricated with processing parameters of $P = 250$ W, $v = 1250$ mm/s, $h = 140$ μm and $t = 30$ μm, which is consistent with our predicted process window, corresponding to the position of the white circle in the solid green zone of Fig. 5(a).

In order to have a more in-depth understanding of the defects formation, the cross-sectional investigation of Nitinol samples manufactured with various L-PBF processing parameters is provided in Fig. 11. As can be seen, the condition of 250/1250 J/mm linear energy density (sample A2 with hatch distance of 120 μm (Fig. 11 (b)), exhibits highest densification and is nearly defect-free. The large hatch distance in A3 resulted in irregular lack of fusion (Fig. 11 (c)). This result is also consistent with our calculated prediction of lack of fusion (Fig. 5(a)). Compared with the sample A2, although there is enough overlapping of laser tracks for avoiding lack-of-fusion in A1, the narrow hatch distance can cause a high volumetric energy density. As a result, vaporization may become severe and cause formation of bubbles. Once the bubbles are trapped within the molten pools, pores can be formed [61].

Another sample featuring lack of fusion defect is sample A9 (Fig. 11 (f)). Referring to the processing maps (Fig. 5(b)), the position of sample A9 is located in the region where lack of fusion is expected (solid green region is the fully dense region, in the condition of $h = 187$ and $t = 30$ μm). This indicates that the processing map can give a relatively good estimation on the occurrence of lack of fusion.

3.6. Cracks in L-PBF nitinol

Besides balling, keyhole-induced pores and lack of fusion, cracks in L-PBF Nitinol parts cannot be tolerated. As shown in the top-view (Fig. 8 and Fig. 9) and cross-sectional representation (Fig. 11), cracks usually exist in L-PBF Nitinol samples with high volumetric energy densities (>74 J/mm^3). These high volumetric energy densities originate either from high linear energy densities or large overlapping of laser tracks (Fig. 12 (a) and (b)), resulting from relatively low hatch distances.

With increasing linear energy density to 250/800 (J/mm), cracks become dominant defects for samples A4 (Fig. 9(a) and (d), and Fig. 11 (d)) and A5 (Fig. 8(b) and (e), and Fig. 11 (e)) with hatch distance of 120 and 140 μm, respectively. As expected, with further increasing linear energy density to 250/600 J/mm, cracks are produced, as demonstrated in A7 sample (Fig. 8(c) and (f), Fig. 11 (g), and Fig. 12 (a)).

During cooling the deposited bead will experience solidification and thermal contraction, combined with transformation strains. If the induced strain exceeds a critical strain the material will crack. Therefore, larger beads, related to higher linear energy density are more susceptible to hot-cracking. However, the strain rate also affects crack formation and is determined by the cooling rate, which also depends on the linear energy density. A lower strain rate, associated with a higher linear energy density improves the crack resistance. Therefore, both total strain and strain rate should be considered for crack sensitivity of the material.

It also should be noted that phase transformation and detwinning can be triggered by residual stress [62], as a result of the shape memory property of Nitinol alloys, which brings a challenge and complexity in evaluation of residual stress in Nitinol alloys. Although it is not the scope of this work it would be interesting to investigate these observations by experimental measurements of residual 3D stress in the L-PBF Nitinol parts.

Therefore, considering defects of balling, keyhole-induced pores, lack of fusion and cracks together, the best quality among all studied herein process groups was found for A2 sample featuring a moderate hatch distance of 120 μm, which is consistent with the density measurements (Fig. 6).

Although the developed herein processability maps do not show the boundary conditions for cracks formation, it still can be successfully applied with respect to balling, keyhole-induced pores and lack of fusion (Fig. 5). Furthermore, by combining with the experimental results, it has been demonstrated that a low linear energy density contributes to

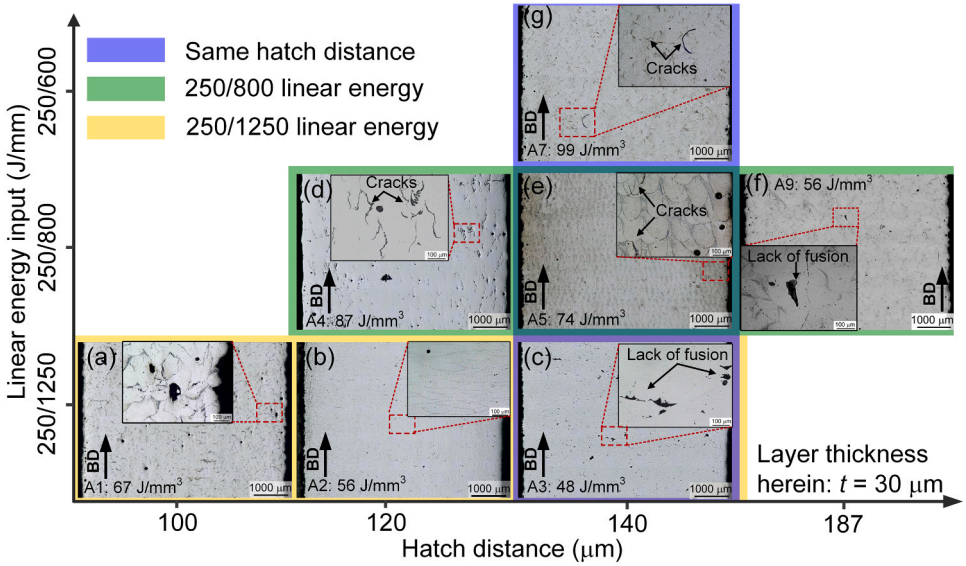

Fig. 11. SEM of cross sections of L-PBF Nitinol alloys fabricated with various processing parameters.

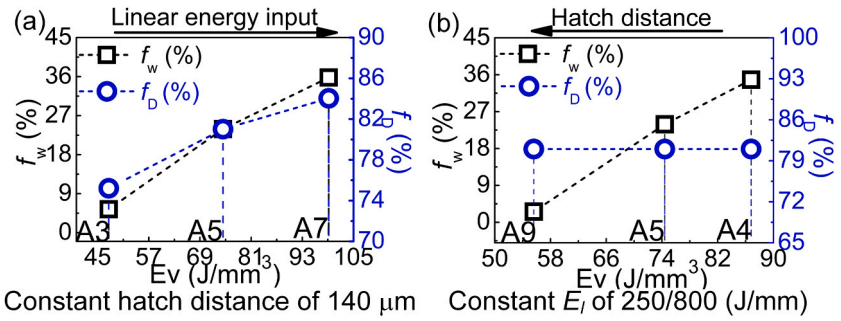

Fig. 12. Overlapping ratios of melt pool width and height of various samples: (a) samples with constant hatch distance of 140 μm but various linear energy densities; (b) samples with constant linear energy density of 250/800 (J/mm) but various hatch distances ranging from 120 to 187 μm.

avoiding the formation of cracks. Therefore, defect-free Nitinol samples can be fabricated by choosing a low linear energy density in the good zone of process maps (the good zone is surrounded by solid blue line in Fig. 5(a)).

3.7. Hardness, martensite phase transformation temperatures and Ni contents

In order to evaluate the processability of L-PBF Nitinol alloys, it is important to consider its properties, such as hardness, shape memory effect, and superelasticity [63]. Hardness measurements were conducted in this work as it can provide a quick and direct evaluation of densification. In addition to Nitinol hardness, the martensite starting temperature (M_s) determine the operating temperatures of Nitinol alloys. Therefore, it is crucial to understand the relationship between M_s and the L-PBF processing conditions. As depicted in Fig. 13, the hardness generally decreases with increasing volumetric (from 240 to 190 HV, Fig. 13 (a)) and linear energy density (from 240 to 203 HV, Fig. 13 (b)). In contrast, the M_s increase from 55 to 67 °C with the increase of energy density (for both E_v and E_l). The reason for the changing trend of hardness is that high energy density (E_v > 56 J/mm^3 and E_l > 250/1250 J/mm) results in large grain sizes [64], which causes the decrease of hardness. An exception is observed in sample A3 (Fig. 13 (a)), where a lower hardness was achieved with decreasing E_v to 48 J/mm^3. The low hardness in the sample A3 is attributed to the occurrence lack of fusion (Fig. 7(c) and Fig. 11 (c)). Fig. 13 presents the micro-hardness measurements results, which vary between 190 and 240 HV among all samples. On the whole, these values are comparable with the hardness of Nitinol fabricated by conventional extrusion methods (~219 – 227 HV) [65].

As shown in Fig. 14, with increasing the volumetric energy density, the Ni content decreases. It indicates that more pronounced evaporation occurs at higher energy densities which has also been reported by previous research [28,35]. Since phase transformation temperatures of Nitinol increase with decreasing Ni content, there is an upward trend of M_s as a function of energy density. Hence, the lower the Ni content (with higher energy densities) the higher M_s temperature (see Fig. 13 and Fig. 14). In this work, the outlier A6 with the highest linear energy density of 250/500 (J/mm) among all studied herein samples has a relatively high M_s temperature due to a higher Ni evaporation, as seen in Fig. 14.

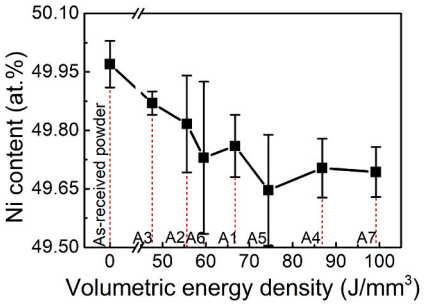

Fig. 14. the Ni content as a function of volume energy density.

It should be noted that sample A3 also shows an abnormal M_s temperature compared with the general upward trend of M_s temperature (Fig. 13 (a)). Sample A3 compared to sample A2, has a larger hatch distance of 140 μm. As reported by Ma et al. [6], increasing hatch distance can introduce high dislocation density in Nitinol samples, and the M_s temperature decreases with an increasing dislocation density due to introduction of more local misfits during phase transformations [66]. In addition, residual stresses, which are inevitable in L-PBF process due to high heating and cooling rates [5], can increase the transformation temperature of Nitinol alloys [67]. Hence, both high dislocation density and residual stress could also contribute to the increase in M_s temperature.

More work regarding microstructure and texture evolution, as well as characterization of mechanical and functional properties of samples studied in this work will be further investigated in our follow up publication.

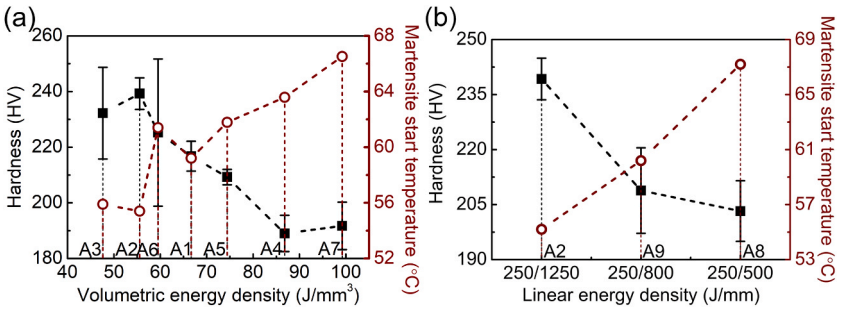

Fig. 13. Micro-hardness of L-PBF samples as a function of (a) volumetric energy density and (b) linear energy density.

4. Conclusions

In this work we demonstrated the feasibility of analytical models for predicting melt pool dimensions of L-PBF Nitinol. Based on analytical solutions of the melt pool dimensions and defect formation criteria, L-BPF processing maps for fabricating Nitinol alloys were drawn. The reliability of the L-BPF processing maps was validated for Nitinol fabricated by different L-BPF processing conditions. The main conclusions of this work can be summarized as follows:

1. Fully dense L-PBF Nitinol parts (>99%) can be successfully fabricated by utilizing the analytically developed processing maps. However, cracks should be separately considered and can be inhibited by adopting desirable overlapping ratios of laser tracks and linear energy density.
2. Heat input related parameters, such as laser power and scanning velocity should be carefully chosen to achieve defect-free laser tracks. With a laser power of 250 W, scanning velocity should be higher than 500 mm/s to avoid keyholing and lower than 1250 mm/s to prevent Nitinol parts from balling. Balling can be reduced by increasing hatch distance, but there was nearly no effect found on keyholing with changing hatch distance and layer thickness.
3. Hardness and M_s of L-PBF Nitinol alloys was found to be sensitive to energy density (including both E_v and E_l). Hardness shows a decrease from 240 to 190 HV with increasing E_v from 56 to 99 J/mm^3. M_s shows an upward trend with increasing energy density, which increases from 55 to 67 °C. The increase phase transformation temperatures is mainly attributed to Nickel evaporation during L-PBF.

Thus, in this work we demonstrated the use of proposed analytical approaches for development and optimization of process parameters (including laser power, scanning velocity, hatch distance and layer thickness) for L-PBF fabrication of defect-free Nitinol alloys.

To further this work, a comprehensive study should be conducted to evaluate the influence of processing parameters of microstructure, texture, mechanical and shape memory characteristics. Furthermore, besides Ni/Ti chemical composition ratio, the shape memory properties of Nitinol also depend on grain characteristics and crystal defects (vacancies, dislocations, and precipitates), which can be affected by the complex thermal history of L-PBF processing. Our upcoming works will aim to understand these relations in L-PBF Nitinol alloys.

CRediT authorship contribution statement

Jia-Ning Zhu: Conceptualization, Methodology, Formal analysis, Experimental validation, Writing - original draft. **Evgenii Borisov:** Methodology, Writing - review & editing. **Xiaohui Liang:** Conceptualization, Software, Writing - review & editing **Eduard Farber:** Methodology and Writing - review & editing. **M.J.M. Hermans:** Supervision, Resources, Writing - review & editing. **V.A. Popovich:** Conceptualization, Supervision, Resources, Funding acquisition, Project administration, Writing - review & editing.

Declaration of Competing Interest

The authors declare that they have no known competing financial interests or personal relationships that could have appeared to influence the work reported in this paper.

Acknowledgments

We acknowledge the support from the Russian Science Foundation grant (project No. 19–79-30002). Jia-Ning Zhu wish to thank the China Scholarship Council (CSC) for financial support. The valuable suggestions and discussions about Analytical models from Dr. Fei-Yu Wang are greatly acknowledged.

References

[1] J. Mohd Jani, M. Leary, A. Subic, M.A. Gibson, A review of shape memory alloy research, applications and opportunities, Mater. Des. 56 (1980–2015) (2014) 1078–1113.
[2] N. Shayesteh Moghaddam, S.E. Saghaian, A. Amerinatanzi, H. Ibrahim, P. Li, G. P. Toker, H.E. Karaca, M. Elahinia, Anisotropic tensile and actuation properties of NiTi fabricated with selective laser melting, Mater. Sci. Eng. A 724 (2018) 220–230.
[3] K. Weinert, V. Petzoldt, Machining of NiTi based shape memory alloys, Mater. Sci. Eng. A 378 (1) (2004) 180–184.
[4] G. Peduk, S. Dilibal, O. Harrysson, S. Özbek, Comparison of the production processes of nickeltitanium shape memory alloy through additive manufacturing, Int. Symp. 3D Print. Addit. Manuf. (2017).
[5] M. Elahinia, N. Shayesteh Moghaddam, M. Taheri Andani, A. Amerinatanzi, B. A. Bimber, R.F. Hamilton, Fabrication of NiTi through additive manufacturing: a review, Prog. Mater. Sci. 83 (2016) 630–663.
[6] J. Ma, B. Franco, G. Tapia, K. Karayagiz, L. Johnson, J. Liu, R. Arroyave, I. Karaman, A. Elwany, Spatial control of functional response in 4D-printed active metallic structures, Sci. Rep. 7 (1) (2017), 46707.
[7] Z.X. Khoo, Y. Liu, J. An, C.K. Chua, Y.F. Shen, C.N. Kuo, A review of selective laser melted niti shape memory alloy, Materials 11 (4) (2018), 519.
[8] M.H. Nasab, D. Gastaldi, N.F. Lecis, M. Vedani, On morphological surface features of the parts printed by selective laser melting (SLM), Addit. Manuf. 24 (2018) 373–377.
[9] B. Zhang, Y. Li, Q. Bai, Defect formation mechanisms in selective laser melting: a review, Chin. J. Mech. Eng. 30 (3) (2017) 515–527.
[10] J.-B. Forien, N.P. Calta, P.J. DePond, G.M. Guss, T.T. Roehling, M.J. Matthews, Detecting keyhole pore defects and monitoring process signatures during laser powder bed fusion: a correlation between in situ pyrometry and ex situ X-ray radiography, Addit. Manuf. 35 (2020), 101336.
[11] N.J. Harrison, I. Todd, K. Mumtaz, Reduction of micro-cracking in nickel superalloys processed by Selective Laser Melting: a fundamental alloy design approach, Acta Mater. 94 (2015) 59–68.
[12] I. Yadroitsev, A. Gusarov, I. Yadroitsava, I. Smurov, Single track formation in selective laser melting of metal powders, J. Mater. Process. Technol. 210 (12) (2010) 1624–1631.
[13] A. Sola, A. Nouri, Microstructural porosity in additive manufacturing: the formation and detection of pores in metal parts fabricated by powder bed fusion, J. Adv. Manuf. Process. 1 (3) (2019), e10021.
[14] G. Kasperovich, J. Haubrich, J. Gussone, G. Requena, Correlation between porosity and processing parameters in TiAl6V4 produced by selective laser melting, Mater. Des. 105 (2016) 160–170.
[15] J. Braun, L. Kaserer, J. Stajkovic, K.H. Leitz, B. Tabernig, P. Singer, P. Leibenguth, C. Gspan, H. Kestler, G. Leichtfried, Molybdenum and tungsten manufactured by selective laser melting: analysis of defect structure and solidification mechanisms, Int. J. Refract. Met. Hard Mater. 84 (2019), 104999.
[16] J. Walker, M. Elahinia, C. Haberland, An Investigation of Process Parameters on Selective Laser Melting of Nitinol, ASME 2013 Conference on Smart Materials, Adaptive Structures and Intelligent Systems, 2013.
[17] C. Zhao, H. Liang, S. Luo, J. Yang, Z. Wang, The effect of energy input on reaction, phase transition and shape memory effect of NiTi alloy by selective laser melting, J. Alloy. Compd. 817 (2020), 153288.
[18] U. Scipioni Bertoli, A.J. Wolfer, M.J. Matthews, J.-P.R. Delplanque, J. M. Schoenung, On the limitations of volumetric energy density as a design parameter for Selective Laser Melting, Mater. Des. 113 (2017) 331–340.
[19] J.P. Oliveira, A.D. LaLonde, J. Ma, Processing parameters in laser powder bed fusion metal additive manufacturing, Mater. Des. 193 (2020), 108762.
[20] I. Yadroitsev, I. Yadroitsava, P. Bertrand, I. Smurov, Factor analysis of selective laser melting process parameters and geometrical characteristics of synthesized single tracks, Rapid Prototyp. J. 18 (3) (2012) 201–208.
[21] L. Wang, Q.S. Wei, Y.S. Shi, J.H. Liu, W.T. He, Experimental investigation into the single-track of selective laser melting of IN625, Adv. Mater. Res. 233–235 (2011) 2844–2848.
[22] D. Gu, Y. Shen, Balling phenomena in direct laser sintering of stainless steel powder: metallurgical mechanisms and control methods, Mater. Des. 30 (8) (2009) 2903–2910.
[23] R. Cunningham, C. Zhao, N. Parab, C. Kantzos, J. Pauza, K. Fezzaa, T. Sun, A. D. Rollett, Keyhole threshold and morphology in laser melting revealed by ultrahigh-speed x-ray imaging, Science 363 (6429) (2019) 849–852.
[24] C. Haberland, M. Elahinia, J.M. Walker, H. Meier, J. Frenzel, On the development of high quality NiTi shape memory and pseudoelastic parts by additive manufacturing, Smart Mater. Struct. 23 (10) (2014), 104002.
[25] E. Farber, J.-N. Zhu, A. Popovich, V. Popovich, A review of NiTi shape memory alloy as a smart material produced by additive manufacturing, Mater. Today Proc. (2020).
[26] C. Haberland, H. Meier, J. Frenzel, On the properties of Ni-rich NiTi shape memory parts produced by selective laser melting, ASME 2012 Conference on Smart Materials, Adaptive Structures and Intelligent Systems, SMASIS 2012, 2012, pp. 97–104.
[27] H. Meier, C. Haberland, J. Frenzel, Structural and functional properties of NiTi shape memory alloys produced by Selective Laser Melting, Innovative Developments in Virtual and Physical Prototyping - Proceedings of the 5th International Conference on Advanced Research and Rapid Prototyping, 2012, pp. 291–296.

[28] S. Saedi, N. Shayesteh Moghaddam, A. Amerinatanzi, M. Elahinia, H.E. Karaca, On the effects of selective laser melting process parameters on microstructure and thermomechanical response of Ni-rich NiTi, Acta Mater. 144 (2018) 552–560.
[29] S. Dadbakhsh, M. Speirs, J.-P. Kruth, J. Schrooten, J. Luyten, J. Van Humbeeck, Effect of SLM parameters on transformation temperatures of shape memory nickel titanium parts, Adv. Eng. Mater. 16 (9) (2014) 1140–1146.
[30] J.P. Oliveira, T.G. Santos, R.M. Miranda, Revisiting fundamental welding concepts to improve additive manufacturing: from theory to practice, Prog. Mater. Sci. 107 (2020), 100590.
[31] K.G. Prashanth, S. Scudino, T. Maity, J. Das, J. Eckert, Is the energy density a reliable parameter for materials synthesis by selective laser melting? Mater. Res. Lett. 5 (6) (2017) 386–390.
[32] M. Letenneur, A. Kreitcberg, V. Brailovski, Optimization of laser powder bed fusion processing using a combination of melt pool modeling and design of experiment approaches: density control, J. Manuf. Mater. Process. 3 (1) (2019) 21.
[33] R. Seede, D. Shoukr, B. Zhang, A. Whitt, S. Gibbons, P. Flater, A. Elwany, R. Arroyave, I. Karaman, An ultra-high strength martensitic steel fabricated using selective laser melting additive manufacturing: Densification, microstructure, and mechanical properties, Acta Mater. 186 (2020) 199–214.
[34] S. Dadbakhsh, M. Speirs, J. Van Humbeeck, J.-P. Kruth, Laser additive manufacturing of bulk and porous shape-memory NiTi alloys: from processes to potential biomedical applications, MRS Bull. 41 (10) (2016) 765–774.
[35] L. Johnson, M. Mahmoudi, B. Zhang, R. Seede, X. Huang, J.T. Maier, H.J. Maier, I. Karaman, A. Elwany, R. Arróyave, Assessing printability maps in additive manufacturing of metal alloys, Acta Mater. 176 (2019) 199–210.
[36] P. Promoppatum, S.-C. Yao, Analytical evaluation of defect generation for selective laser melting of metals, Int. J. Adv. Manuf. Technol. 103 (1–4) (2019) 1185–1198.
[37] M. Tang, P.C. Pistorius, J.L. Beuth, Prediction of lack-of-fusion porosity for powder bed fusion, Addit. Manuf. 14 (2017) 39–48.
[38] C. Teng, D. Pal, H. Gong, K. Zeng, K. Briggs, N. Patil, B. Stucker, A review of defect modeling in laser material processing, Addit. Manuf. 14 (2017) 137–147.
[39] G.G. Gladush, I. Smurov, Physics of Laser Materials Processing: Theory and Experiment, Springer Science & Business Media, 2011.
[40] K. Tolochko Nikolay, E. Mozzharov Sergei, A. Yadroitsev Igor, T. Laoui, L. Froyen, I. Titov Victor, B. Ignatiev Michail, Balling processes during selective laser treatment of powders, Rapid Prototyp. J. 10 (2) (2004) 78–87.
[41] A.A. Martin, N.P. Calta, S.A. Khairallah, J. Wang, P.J. Depond, A.Y. Fong, V. Thampy, G.M. Guss, A.M. Kiss, K.H. Stone, C.J. Tassone, J. Nelson Weker, M. F. Toney, T. van Buuren, M.J. Matthews, Dynamics of pore formation during laser powder bed fusion additive manufacturing, Nat. Commun. 10 (1) (2019) 1987.
[42] B. Zhou, J. Zhou, H. Li, F. Lin, A study of the microstructures and mechanical properties of Ti6Al4V fabricated by SLM under vacuum, Mater. Sci. Eng. A 724 (2018) 1–10.
[43] J. Zhou, H.-L. Tsai, Effects of electromagnetic force on melt flow and porosity prevention in pulsed laser keyhole welding, Int. J. Heat. Mass Transf. 50 (11) (2007) 2217–2235.
[44] S. Leuders, M. Thöne, A. Riemer, T. Niendorf, T. Tröster, H.A. Richard, H.J. Maier, On the mechanical behaviour of titanium alloy TiAl6V4 manufactured by selective laser melting: fatigue resistance and crack growth performance, Int. J. Fatigue 48 (2013) 300–307.
[45] H. Gong, K. Rafi, H. Gu, G.D. Janaki Ram, T. Starr, B. Stucker, Influence of defects on mechanical properties of Ti–6Al–4V components produced by selective laser melting and electron beam melting, Mater. Des. 86 (2015) 545–554.
[46] W. Ke, X. Bu, J.P. Oliveira, W. Xu, Z. Wang, Z. Zeng, Modeling and numerical study of keyhole-induced porosity formation in laser beam oscillating welding of 5A06 aluminum alloy, Opt. Laser Technol. 133 (2021), 106540.
[47] D.B. Hann, J. Iammi, J. Folkes, A simple methodology for predicting laser-weld properties from material and laser parameters, J. Phys. D Appl. Phys. 44 (44) (2011), 445401.
[48] A.M. Rubenchik, W.E. King, S.S. Wu, Scaling laws for the additive manufacturing, J. Mater. Process. Technol. 257 (2018) 234–243.
[49] T.W. Eagar, N.S. TSAi, Temperature fields produced by traveling distributed heat sources, Weld. J. 62 (12) (1983) 346–355.
[50] K.-H. Lee, G.J. Yun, A novel heat source model for analysis of melt Pool evolution in selective laser melting process, Addit. Manuf. 36 (2020), 101497.
[51] K. Otsuka, X. Ren, Physical metallurgy of Ti–Ni-based shape memory alloys, Prog. Mater. Sci. 50 (5) (2005) 511–678.
[52] F. Verhaeghe, T. Craeghs, J. Heulens, L. Pandelaers, A pragmatic model for selective laser melting with evaporation, Acta Mater. 57 (20) (2009) 6006–6012.
[53] Y.S. Lee, W. Zhang, Modeling of heat transfer, fluid flow and solidification microstructure of nickel-base superalloy fabricated by laser powder bed fusion, Addit. Manuf. 12 (2016) 178–188.
[54] H. Fang, M.B. Wong, Y. Bai, R. Luo, Effect of heating/cooling rates on the material properties of NiTi wires for civil structural applications, Constr. Build. Mater. 101 (2015) 447–455.
[55] C. Zanotti, P. Giuliani, P. Bassani, Z. Zhang, A. Chrysanthou, Comparison between the thermal properties of fully dense and porous NiTi SMAs, Intermetallics 18 (1) (2010) 14–21.
[56] C. Zanotti, P. Giuliani, G. Riva, A. Tuissi, A. Chrysanthou, Thermal diffusivity of Ni–Ti SMAs, J. Alloy. Compd. 473 (1–2) (2009) 231–237.
[57] J.W. Mwangi, L.T. Nguyen, V.D. Bui, T. Berger, H. Zeidler, A. Schubert, Nitinol manufacturing and micromachining: a review of processes and their suitability in processing medical-grade nitinol, J. Manuf. Process. 38 (2019) 355–369.
[58] G.R. Mirshekari, A. Saatchi, A. Kermanpur, S.K. Sadrnezhaad, Laser welding of NiTi shape memory alloy: comparison of the similar and dissimilar joints to AISI 304 stainless steel, Opt. Laser Technol. 54 (2013) 151–158.
[59] X.P. Li, K.M. O'Donnell, T.B. Sercombe, Selective laser melting of Al-12Si alloy: Enhanced densification via powder drying, Addit. Manuf. 10 (2016) 10–14.
[60] J.H. Martin, B.D. Yahata, J.M. Hundley, J.A. Mayer, T.A. Schaedler, T.M. Pollock, 3D printing of high-strength aluminium alloys, Nature 549 (7672) (2017) 365–369.
[61] Y.H. Zhou, W.P. Li, L. Zhang, S.Y. Zhou, X. Jia, D.W. Wang, M. Yan, Selective laser melting of Ti–22Al–25Nb intermetallic: significant effects of hatch distance on microstructural features and mechanical properties, J. Mater. Process. Technol. 276 (2020), 116398.
[62] Q. Zhou, M.D. Hayat, G. Chen, S. Cai, X. Qu, H. Tang, P. Cao, Selective electron beam melting of NiTi: Microstructure, phase transformation and mechanical properties, Mater. Sci. Eng. A 744 (2019) 290–298.
[63] S. Shiva, I.A. Palani, S.K. Mishra, C.P. Paul, L.M. Kukreja, Investigations on the influence of composition in the development of Ni–Ti shape memory alloy using laser based additive manufacturing, Opt. Laser Technol. 69 (2015) 44–51.
[64] T. Larimian, M. Kannan, D. Grzesiak, B. AlMangour, T. Borkar, Effect of energy density and scanning strategy on densification, microstructure and mechanical properties of 316L stainless steel processed via selective laser melting, Mater. Sci. Eng. A 770 (2020), 138455.
[65] J. Luo, J.O. Bobanga, J.J. Lewandowski, Microstructural heterogeneity and texture of as-received, vacuum arc-cast, extruded, and re-extruded NiTi shape memory alloy, J. Alloy. Compd. 712 (2017) 494–509.
[66] M.F.X. Wagner, S.R. Dey, H. Gugel, J. Frenzel, C. Somsen, G. Eggeler, Effect of low-temperature precipitation on the transformation characteristics of Ni-rich NiTi shape memory alloys during thermal cycling, Intermetallics 18 (6) (2010) 1172–1179.
[67] J.P. Oliveira, A.J. Cavaleiro, N. Schell, A. Stark, R.M. Miranda, J.L. Ocana, F. M. Braz Fernandes, Effects of laser processing on the transformation characteristics of NiTi: a contribute to additive manufacturing, Scr. Mater. 152 (2018) 122–126.